**Batteries & Supercaps**

Research Article
doi.org/10.1002/batt.202500014

**Chemistry Europe**
European Chemical Societies Publishing

www.batteries-supercaps.org

# Synergistic Improvements in Ionic Conductivity, Diffusion Dynamics, and Transference Numbers for LaNiO₃/MXene Supercapacitor Electrodes

Abdul Shakoor, Muhammad Adnan, Muhammad Luqman, Muhammad Ahmed Khan, Shahid M. Ramay, Farooq Ahmad,* and Shahid Atiq*

Supercapacitors are crucial for bridging energy storage gaps, offering rapid charge/discharge rates, long cycle life, and high power density, key for renewable energy systems and electric vehicles. This study incorporated MXene ($Ti_3C_2T_x$) into $LaNiO_3$ (PLNO) at 0, 10, 20, and 30 wt% via solvothermal synthesis. X-ray diffraction confirmed a simple cubic phase across all samples. BET analysis and FESEM revealed mesoporous structures and reduced grain sizes due to MXene inclusion, contributing to enhanced electrochemical performance. Elemental analysis via EDS matched expected stoichiometry. Cyclic voltammetry indicated battery-type behavior, with the LNO-III sample achieving the highest capacity of 541.60 C g$^{-1}$ at 2.5 mV s$^{-1}$. Galvanostatic charge/discharge profiles showed increasing discharge times with higher MXene content. The Ragone plot highlighted excellent energy and power densities of 84.30 Wh kg$^{-1}$ and 2125 W kg$^{-1}$ at 2.5 A g$^{-1}$. Long-term testing demonstrated strong cycle stability, with 88.12% retention over 10 000 cycles. Electrochemical impedance spectroscopy showed low charge transfer resistance (0.84 Ω), short relaxation time (17 ms), high ion diffusion rate ($9.5 \times 10^{-13}$ m$^2$ s$^{-1}$), good ionic conductivity ($6.3 \times 10^{-3}$ S cm$^{-1}$), and a transference number (t$_+$) of 0.3. These results confirm the potential of MXene-modified PLNO as a promising electrode for high-performance supercapacitors.

## 1. Introduction

The explosive growth of the population, the relentless depletion of fossil fuels, and rapid technological advancements have combined to create severe pollution and energy crises. Researchers worldwide have recognized an urgent need for sustainable energy solutions to address these issues and have turned to clean and renewable energy resources.[1–6] However, these energy resources require efficient storage solutions, paving the way for advancements in electrochemical energy storage devices (EESDs). These EESDs are crucial in addressing the energy crisis by efficiently bridging the gap between energy production and consumption, integrating renewable sources, and ensuring a stable and reliable power supply.[7] Among all EESDs,

supercapacitors (SCs) have witnessed significant research advancements, inheriting features such as rapid charging and discharging rates, outstanding power density, long-term cost savings, and environmental sustainability due to their extended lifespan and use of eco-friendly materials. Due to these characteristics, SCs are considered promising candidates for providing instant energy, offering a hopeful future for energy storage solutions.[8–11]

In SCs, the charge storage mechanism is the most significant aspect, and based on this, SCs are further classified into three major categories: 1) electric double-layer capacitors (EDLCs), 2) pseudo capacitors (PCs), and 3) hybrid capacitors.[12] Likewise, the choice of electrode material plays a vital role in determining the rate performance of SCs. For EDLCs, carbonaceous compounds are preferred, as charges are stored electrostatically, forming a double layer that yields high PD.[13] In PCs, hydroxides and transition metal oxides are considered to favor redox reactions following the Faradaic processes.[14] Composite hybrids are preferred for hybrid capacitors, indicating that charges are being stored both electrostatically and electrochemically, yielding a reasonable energy density (ED) and excellent PD compared to other capacitors.[15,16]

To date, various two-dimensional (2D) materials have been explored to assess their electrochemical performance; among them, researchers have recently developed an efficient and novel class of 2D metal carbides/nitrides, or carbonitrides known as MXene, in 2011. Generally, $M_{n+1}X_nT_x$ is the general formula of MXene materials in which $M$ belongs to the early transition metals. Meanwhile, $X$ and $T_x$ reflect the nitrogen or carbon and surface termination groups, that is =O, −F, −OH, and so on depending

*A. Shakoor, M. Adnan, M. Luqman, M. Ahmed Khan, F. Ahmad, S. Atiq*
*Centre of Excellence in Solid State Physics*
*University of the Punjab*
*Lahore 54590, Pakistan*
*E-mail: farooq.ahmad@ifmpan.poznan.pl*
        *satiq.cssp@pu.edu.pk*

*S. M. Ramay*
*Physics and Astronomy Department*
*College of Science*
*King Saud University*
*P.O. Box 2455, Riyadh 11451, Saudi Arabia*

*F. Ahmad*
*Polish Academy of Sciences*
*Institute of Molecular Physics*
*M. Smoluchowskiego 17, 60-179 Poznań, Poland*

**Batteries & Supercaps**

Research Article
doi.org/10.1002/batt.202500014

**Chemistry Europe**
European Chemical
Societies Publishing

upon the etchant used as a surface terminator, while $x$ shows the number of surface functionalities and $n$ ($n = 1$–3), represents the atomic layers. The variation in the value of $n$ from 1–3 alters the general formula of MXene from $M_2CT_x$ to $M_3C_2T_x$ and $M_4C_3T_x$. More than 30 MXenes have been successfully synthesized from 100 MAX phases. Moreover, MXene has more significant potential for use as an electrode material in SC applications due to its outstanding mechanical flexibility and conductivity of up to 25 000 S cm$^{-1}$ compared to graphene.[17] It also features a high specific surface area (SSA), tunable surface chemistry that reflects tunable surface defects, low diffusion barriers, high hydrophilicity, and remarkable intercalation characteristics due to its unique layered structure, offering a promising candidate for future energy storage applications.[18,19]

Despite its numerous features, MXene has some drawbacks, including layer stacking, scalability, and stability challenges, as well as surface functionalities that hinder its exceptional electrochemical response. To address such faults, the scientific community has developed binary MXene into composite MXene, for instance, by incorporating carbonaceous materials, metal oxides, transition metal dichalcogenides, and perovskite oxides. Specifically, perovskite oxides ($ABO_3$-type), like $LaMnO_3$, $LaNiO_3$, $LaFeO_3$, $LaCoO_3$, and so on, demonstrate remarkable electrochemical performance. Due to the variable oxidation states, cost-effectiveness, tunable electronic structure, significant electron mobility, semiconducting nature, and oxygen vacancies of transition metals have gained substantial attention in the last few years by researchers worldwide.[20,21]

It is evident from the last literature surveys that SCs have shown low ED, specific capacitance ($C_{sp}$), and SSA compared to batteries, an ongoing challenge that must be addressed.[17,18] At the same time, the key criteria for composite electrode materials include ionic conductivity, transference number, diffusion coefficient, electrochemical stability, and mechanical robustness. However, achieving a combination of all these desirable properties in a single electrode/electrolyte remains a significant challenge. Therefore, MXene/Perovskite-based composites, with unique layered structures, facilitate ion diffusion and long-term performance, tunable surface chemistry of MXene ($Ti_3C_2T_x$) and perovskite materials mainly ($LaCoO_3$, $LaMnO_3$, and $MnFeO_3$) offers high SSA, providing more active sites and highlight significant potential for high performance electrode materials for SC applications.[22–29] Several reports on them are available, confirming their remarkable electrochemical performance and sparking interest in their unique features.[28,29]

For instance, Lai et al. employed a hydrothermal route to prepare pristine MXene, thereby enhancing the electrochemical performance of the electrode material for SC applications. An asymmetric device based on such electrode material was designed, exhibiting a $C_{sp}$ of about 117 F g$^{-1}$ at 0.50 A g$^{-1}$. The tailored device demonstrated the ED and PD values as 23.4 Wh kg$^{-1}$ and 299.8 W kg$^{-1}$, respectively.[30] These values (ED, PD) are significant as they indicate the amount of energy that can be stored and the rate at which it can be delivered, which are crucial factors in the performance of energy storage devices. Similarly, another approach was used by Varghese et al. to enhance the MXene's electrochemical performance, using an

in situ polymerization approach to prepare two MXene-based composites with polypyrrole (PPy) and polyaniline (PANI) separately. They designed a symmetric device, demonstrating a remarkable $C_{sp}$ of ≈430 F g$^{-1}$ and 305 F g$^{-1}$ for PPy and PANI, respectively. Similarly, MXene/PPy has demonstrated an impressive ED of 38 Wh kg$^{-1}$, a PD of 808 W kg$^{-1}$, and 84% capacitance retention after 10 000 cycles.[31] Moreover, Wang et al. followed a hydrothermal synthesis to fabricate MXene/$NiCo_2O_4$, aiming to enhance the performance of the anode material further. The prepared material through this method showcased an excellent $C_{sp}$, ED, and PD of 1025 F g$^{-1}$, 36.67 Wh kg$^{-1}$, and 800 W kg$^{-1}$, respectively. The prepared composite exhibited good capacitance retention of about 88.2% after 5 k cycles.[32] Meanwhile, Nd-doped $LaNiO_3$ prepared by Qayyum et al. through a solgel autocombustion route showed a $C_{sp}$ value of 64.3 F g$^{-1}$ at 10 mV s$^{-1}$. It displayed PD and ED values of 846.5 W kg$^{-1}$ and 20.92 Wh kg$^{-1}$, respectively.[33]

Based on the aforementioned literature surveys, it can be concluded that MXene can substantially enhance the electrochemical performance of electrode materials for SC applications. Using a facile and cost-effective solvothermal approach, its unique layered structure has been successfully integrated with $ABO_3$-type perovskite oxides ($LaNiO_3$). Moreover, pristine $LaNiO_3$ (PLNO) was prepared using the hydrothermal method. The solvothermal method was employed to synthesize $LaNiO_3@Ti_3C_2T_x$ (LNO@MXene) composites with varying MXene weight percentages, including 10, 20, and 30%, which were labeled as LNO-I, LNO-II, and LNO-III, respectively. Our objective is to propose a system with a stable structure, well-defined morphology, and significant porosity while also exhibiting excellent electrochemical properties to achieve high PD and ED. Additionally, the system must demonstrate high ionic conductivity, a favorable diffusion coefficient, and a high cation transference number. By optimizing these parameters, we aim to minimize the concentration gradient at the electrode surface, thereby enhancing overall performance. Before designing a full device, these critical parameters must be thoroughly investigated, as they provide a strong foundation for successful full-cell fabrication.

## 2. Experimental Section

A mono-layered MXene nanosheets were developed after exfoliation of the Al layer from ($Ti_3AlC_2$) MAX powder using acid/fluoride etching. In this context, 0.9 g of LiF was added to 15 mL (0.135 mol) of 9 M HCl and left under stirring for 10 min. Subsequently, 1.0 g of MAX powder was gradually added because of the exothermic nature of the reactions, and the reaction was allowed to run for 24 h at room temperature (RT). In addition, the suspension was washed several times with deionized water (DIW) at 3500 rpm until the supernatant attained a pH of ≈6. Finally, the resultant product was obtained after vacuum drying for 24 h at 120 °C.
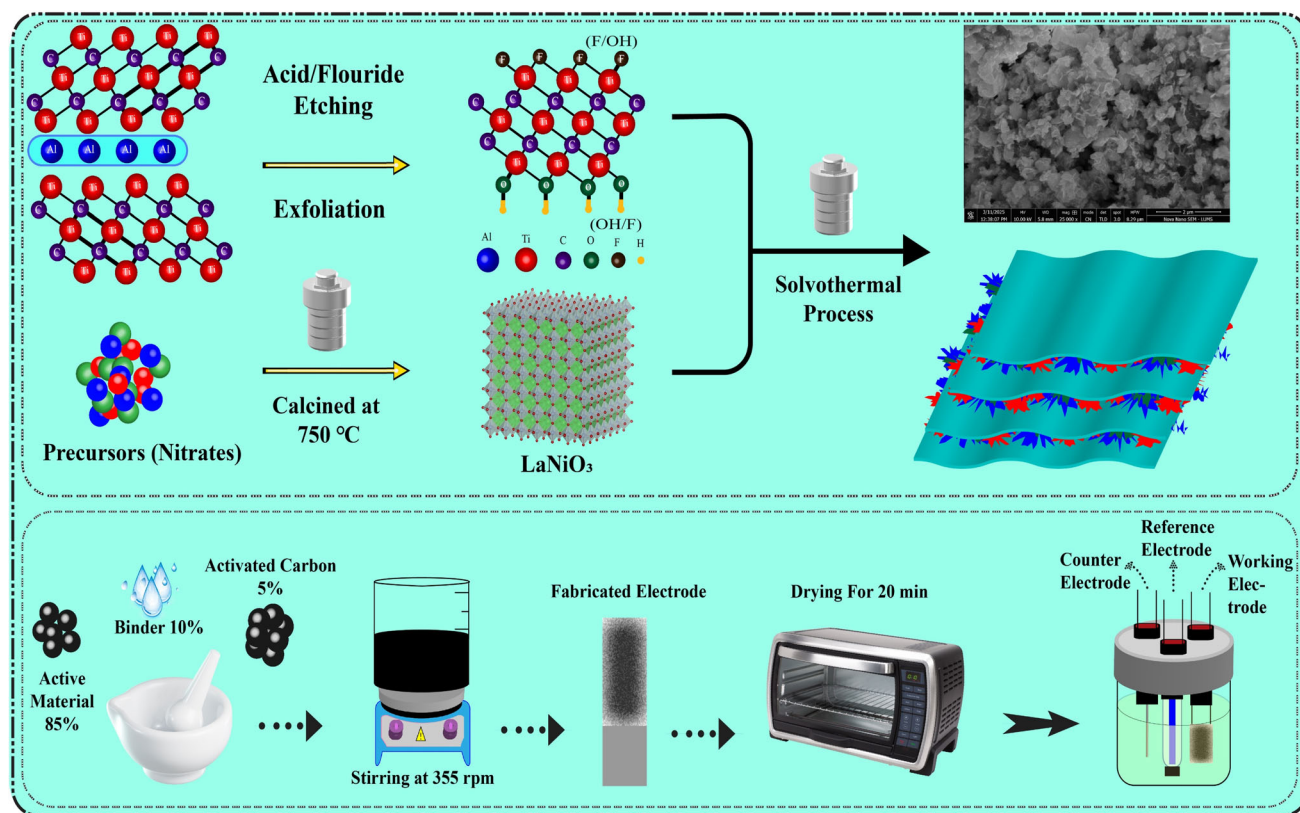
A facile hydrothermal approach was employed to prepare the PLNO. For this purpose, analytical-grade metal nitrate precursors, such as $La(NO_3)_3.6H_2O$ (purity ≥ 99.9%), $Ni(NO_3)_2.6H_2O$ (purity ≥ 98.5%), and KOH, was purchased from Sigma Aldrich.

**Batteries & Supercaps**

Research Article
doi.org/10.1002/batt.202500014

**Chemistry Europe**
European Chemical
Societies Publishing

Stoichiometrically measured amounts of metal nitrates were dissolved in 40 mL of DIW, and the mixture was stirred at 250 rpm to achieve a homogeneous solution. Subsequently, dropwise, 1 M KOH solution was added to speed up the reaction mechanism. The solution was then carefully poured into a Teflon-lined stainless steel autoclave and placed inside the muffle furnace for 3 h at 180 °C. After being cooled down at RT, the suspension was washed thrice with ethanol and DIW to remove the contaminations. Then, the resultant product was dried at 70 °C in an oven. The obtained product was calcined at 750 °C for 4 h in the Nabertherm furnace to remove impurities and ensure crystallinity. The final product was ground using an agate mortar and pastle for 30 min.

The solvothermal route was adopted to prepare the composites. MXene with various weight percentages, such as 10, 20, and 30%, was incorporated with LNO to make three composites. For composite synthesis, the precisely measured quantities of LNO and MXene were dissolved into 40 mL of ethanol. Subsequently, they were subjected to a sonication bath for 1 h at a frequency of 35 kHz to segregate the clusters of nanoparticles. After this, solutions were placed on a hot plate and magnetically stirred at 250 rpm without heating to ensure the homogeneity of phases. The solutions underwent uniform heat treatments using Teflon-lined stainless steel autoclaves, which were then settled in a muffle furnace by constantly heating for 3 h at 180 °C. After the specified duration, the samples were washed thrice with ethanol and DIW. Finally, the resultant products were dried in an oven, and the obtained powders were used as an active electrode material.

The preparation of electrodes involves three significant steps. Initially, it consists of cutting nickel foam (NF), chosen as a substrate, into $1 \times 1.25$ cm pieces. The rationale behind choosing NF is cost-effectiveness with an elevated surface area that develops excellent contact between active material and electrolyte. These pieces were subjected to an etching treatment in an acidic media of 13 mL of HCl (0.156 mol) and 37 mL (2.05 mol) DIW to etch the oxygen layer and other contaminations to enhance the surface roughness. The subsequent step involves the preparation of a binder, where a stoichiometrically weighed amount of polyvinylidene fluoride was dissolved into N-methyle-2-pyrrollidon (NMP). This was then stirred to ensure homogeneity. In the final step, 2 mg of slurry was prepared by mixing the active material (composite), binder, and carbon black with stoichiometric ratios of 85:10:5. Then this mixture was placed on a hotplate (without heating) and stirred for 8 h at 250 rpm. The resulting slurry was applied to NF pieces using a Dragon pipette gun and then dried in an oven at 60 °C for 6 h. **Figure 1** provides a summary of the sample preparation and electrode fabrication process.

To explore the crystalline phase of a series of as-synthesized samples, the X-ray diffraction (XRD) technique was utilized with a Bruker D-8 advanced diffractometer, using a Cu Kα radiation source ($\lambda = 1.54$ Å) with a step size of 0.03°/0.5 s. The morphological properties and element compositions were measured using a Nova Nano-SEM field emission electron microscope (FESEM) endowed with Oxford's instrument energy-dispersive X-ray (EDX) spectroscope. The electrochemical response of the fabricated electrodes was measured using a 3-electrode assembly



**Figure 1.** Schematic profile of sample synthesis and electrode fabrication.

**Batteries & Supercaps**

Research Article
doi.org/10.1002/batt.202500014

**Chemistry Europe**
European Chemical
Societies Publishing

with a 1 M KOH electrolyte, where the counter and reference electrodes were made of Pt wire and Ag/AgCl, respectively. Cyclic voltammetry (CV), galvanostatic charge/discharge (GCD), and electrochemical impedance spectroscopy (EIS) assessments were performed using the CHI 660 E electrochemical workstation (Corrtest Electrochemical & Corrosion Studio, Version 6.4).

## 3. Results and Discussion

To investigate the phase and structural modifications of PLNO, LNO-I, LNO-II, and LNO-III, XRD patterns were collected at $2\theta$ values ranging from 15° to 80°, as illustrated in **Figure 2**a. The diffraction peaks received were indexed using the B.D. Cullity approach.[34] The diffraction peaks observed for PLNO at $2\theta$ values of 23.12°, 32.75°, 40.47°, 46.92°, 52.37°, 58.46°, 68.53°, 73.58°, and 78.21° were associated with lattice planes of (100), (110), (111), (200), (210), (211), (220), (300), and (310), respectively, which were well matched with *ICSD*#00-033-0710. All these facts revealed that PLNO inherits the simple cubic structure with *Pm/3 m* 221 space group. In addition, an additional diffraction peak of MXene appeared at $2\theta$ of 38.37° corresponding to *hkl* (008) with growing intensity, evidencing the variation of MXene's content in three samples, that is LNO-I, LNO-II, and LNO-III, suggesting that MXene possessess crystalline nature with hexagonal structure and belongs to *P6₃/mmc*.[35]

The rationale behind the presence of the (008) peak and the absence of many other peaks corresponding to MXene within the $2\theta$ range of 15° and 80° is that the significantly higher concentration of PLNO compared to MXene highlights the growth of PLNO nanoparticles over the MXene's nanosheets,[36] and hence yielded only the (008) peak due to its highest intensity among the MXene-related peaks in the measured $2\theta$ range under the Bragg's diffraction conditions, which was visible. At the same time, the signals of the other peaks were too weak to be detected against the strong signals of PLNO. On the other hand, the absence of a characteristic peak (002), which typically appears below 9°, is due to the measurement angle being set at 15°; therefore, MXene's prominent peak is not present. Additionally, the XRD patterns of PLNO, MAX phase, and MXene in powder form are depicted in Figure S2a–c, Supporting Information, to verify the phase purity. The characteristic peaks of MXene at 19.23° and 38.37° have been indexed as (004) and (008), as shown in Figure S1c, Supporting Information, indicating the successful formation of the MXene phase.

It can be inferred from the XRD patterns of LNO-I, LNO-II, and LNO-III that only an additional peak due to MXene is observed, while the symmetry of the peaks for PLNO remains unchanged. Figure 2c–e illustrates the structural visualization of PLNO, MXene, and LNO@MXene composite, respectively, by using VESTA structural visualization software, showcasing their intricate architectures with precision and clarity. Furthermore, three more diffraction peaks at $2\theta$ values of 44.79°, 52.01°, and 76.53° were observed, aligning well with *hkl* planes of (111), (200), and (220) which were also obtained and well-coordinated with *ICSD*# 01-070-0989 attributed to nickel, which was used as a substrate. The crystallite size of PLNO, LNO-I, LNO-II, and LNO-III has been tabulated in **Table 1** and depicted in Figure 2b with a 0.4% error bar. It
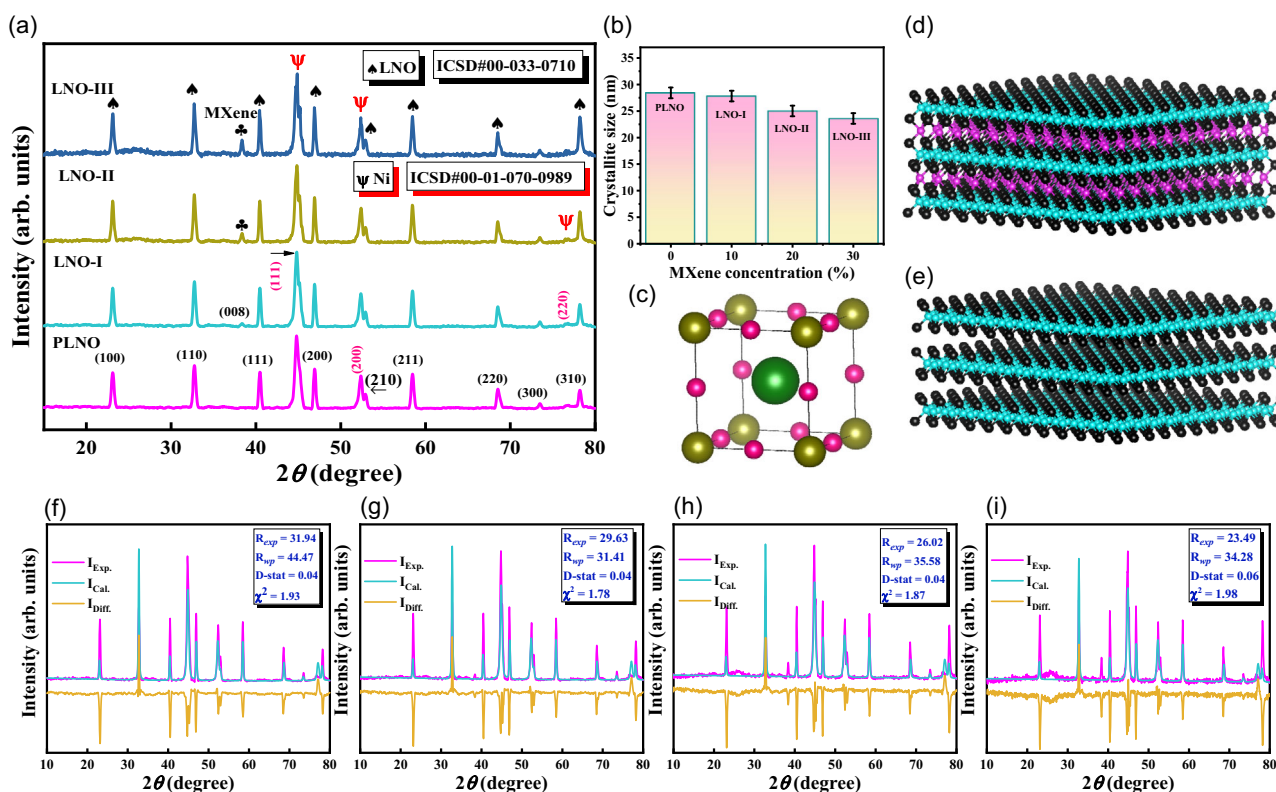


**Figure 2.** a) XRD patterns of PLNO with 0, 10, 20, and 30% addition of MXene, b) crystallite size of all samples, c–e) crystal structure of PLNO, MAX, and MXene, and f–i) Rietveld refinement of all samples.

**Table 1.** Lattice constants, crystallite size, and X-ray and dislocation densities and SSA of all samples.

| Sample | Lattice constant [Å] | Crystallite size [nm] | X-ray density [g cm$^{-3}$] | Dislocation density [nm$^{-2}$] | Specific surface area [m$^2$ g$^{-1}$] |
|---|---|---|---|---|---|
| PLNO | 3.862 | 28.42 | 7.07 | $1.23 \times 10^{-3}$ | 29.81 |
| LNO-I | 3.858 | 27.83 | 7.08 | $1.29 \times 10^{-3}$ | 30.44 |
| LNO-II | 3.857 | 25.01 | 7.09 | $1.59 \times 10^{-3}$ | 33.86 |
| LNO-III | 3.853 | 23.59 | 7.09 | $1.79 \times 10^{-3}$ | 35.87 |

was calculated with the help of Scherrer's equation as 28.42, 27.83, 25.01, and 23.59 nm, respectively, as expressed in Equation (1).

$$D = \frac{0.9\lambda}{\beta \cos\theta} \qquad (1)$$

where $D$ is the crystallite size, $\lambda$ wavelength, $\beta$ full-width half maxima, and $\theta$ is the Bragg's angle. Additionally, lattice parameters and X-ray densities have been evaluated using the general formula ascribed as $a = d\sqrt{h^2 + k^2 + l^2}$ and $\rho_x = NM/N_A V$.

The dislocation density, SSA, and X-ray densities of all samples have been presented in Figure S2a–c, Supporting Information. It can be concluded from this that increasing the MXene content leads to an increase in X-ray and dislocation densities, resulting in enhanced electronic conductivity and improved structural stability, along with increased SSA. The presence of slight noise in all XRD patterns corresponds to the background noise sourced from the X-ray source and the detector's sensitivity. The structural stability of PLNO can be estimated using the Rietveld refinement technique and the value of the tolerance factor, as described.

Rietveld refinement, a powerful tool in materials science, was employed to evaluate the discrepancy between the observed and calculated XRD data using the Xpert HighScore Plus software to ensure accuracy. The goodness of fit, represented as a chi-square value, determines the level of agreement between the experimental and calculated data values. A chi-square value close to 1 indicates a good fit, while a value significantly higher than 1 suggests an inadequate fit. $\chi^2 = R_{wt}/R_{exp}$ determines the level of agreement between experimental and calculated data values. It is evaluated from the ratios of the $R$-weighted profile ($R_{wp}$) to the $R$-expected profile ($R_{exp}$). In this study, the maximum goodness of fit was 1.97 for LNO-III. Such close alignment with unity demonstrates the consistency of previously reported XRD data and currently synthesized samples. Figure 2f–i shows the refinement patterns of PLNO, LNO-I, LNO-II, and LNO-III. It can be observed that the differences in the calculated values are minimal, indicating that the accuracy is high and the structure has been developed perfectly.

For a comprehensive analysis, the Goldschmidt tolerance factor ($t$) is employed to describe the structural stability and distortion of $ABO_3$-type perovskite materials, such as LaNiO$_3$ (PLNO). It also validates whether a perovskite material undergoes structural distortions or perfections. Generally, if the value of $t$ lies between 0.9 and 1, it refers to a stable ideal cubic structure. The following relation (Equation (2)) can be used to assess the structural stability of PLNO

$$t = \frac{r_A + r_X}{\sqrt{2}(r_B + r_X)} \qquad (2)$$

In this equation, $r_A$ stands for the ionic radius of cation at A (La) site perovskite oxide, whereas $r_B$ and $r_X$ represent the ionic radius of the cation at the B (Ni) site and the radius of the anion (Oxygen). The value of t calculated from this equation is 0.97, suggesting the ideal cubic structure of PLNO. Based on this analysis, it can be inferred that PLNO is structurally stable.

The FESEM image in **Figure 3**a shows a sample with a unique combination of well-formed particles and smaller particles, which
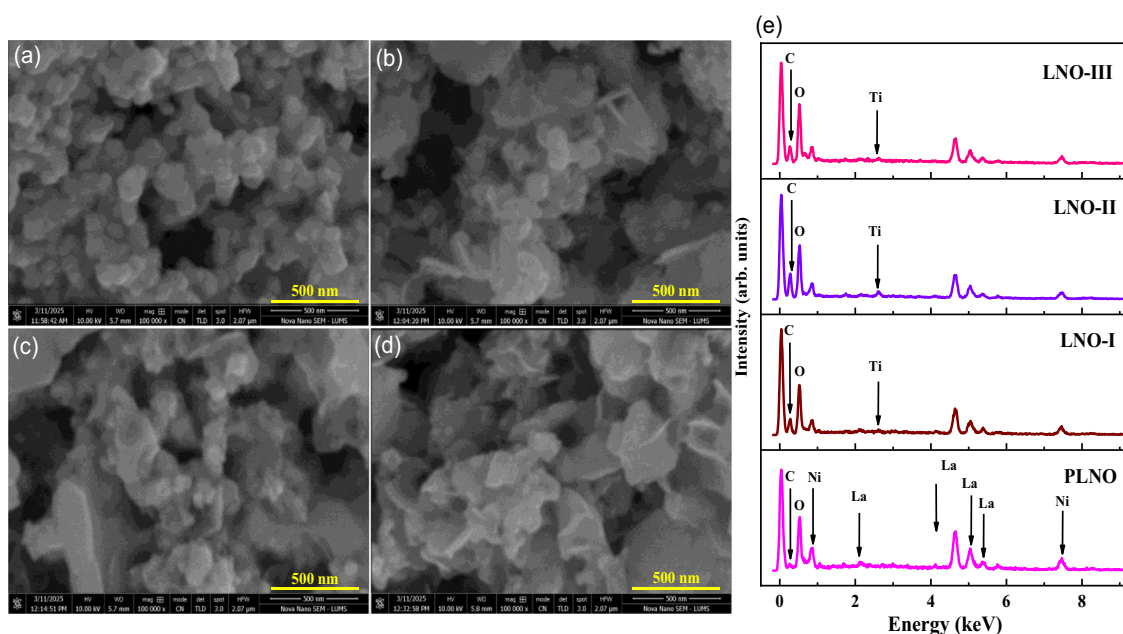


**Figure 3.** a–d) FESEM images of PLNO with 0, 10, 20, and 30% addition of MXene and e) EDX spectra of all samples.

defines the overall morphology. The image also reveals a significant porosity level within the material, as evidenced by visible voids between the grains. While creating a highly porous network, this porosity could be advantageous for electrochemical applications. It offers additional active sites, potentially enhancing the material's electrochemical performance. The irregular distribution pattern, with smaller particles often embedded within larger ones, may limit the effectiveness of the observed voids in facilitating electrochemical reactions due to the interconnected nature of the particles. However, the potential benefits of the observed morphological features are promising for future research and development in this field.

In the context of LNO-I composite materials, the morphological changes observed in the SEM image provide critical insights into the impact of MXene incorporation on the LNO structure (Figure 3b). The image clearly shows the formation of agglomerated small particles, which indicates a notable increase in particle clustering compared to PLNO. This agglomeration is likely due to the introduction of MXene, which influences the overall morphology of the composite. Moreover, distinct 'sepals,' petal-like structures that protrude from the surface, signify the formation of unique structural features not observed in pure LNO. These *sepals*, a unique and intriguing aspect of the composite, likely enhance the composite's surface area, which is crucial for electrochemical applications.

However, the LNO-III sample demonstrates improved electrochemical performance, as evidenced by the morphological features observed in Figure 3d. The image reveals reduced agglomeration compared to previous samples, with more well-defined pores closer to the ideal structure. Additionally, the *sepals* are more clearly visible, indicating a favorable morphology that likely contributes to the enhanced performance of the composite. These morphological characteristics suggest that LNO-III is better optimized for electrochemical applications. It has well-formed pores and distinct *sepals* that resemble blossoming from the flower, which is crucial to its superior behavior, as observed in Figure S3a–d, Supporting Information.

To confirm the composition of the prepared samples, elemental analysis was conducted to determine whether the samples were prepared according to stoichiometric principles. Figure 3e presents the EDX spectra of PLNO and its composites at different doping concentrations (10, 20, and 30%) of MXene. The spectra show characteristic peaks, including those of carbon. Carbon peaks are attributed to the carbon tape used to cover the samples during analysis, indicating that no additional impurities are present in the spectra. Furthermore, Figure 3e provides a detailed overview of the elemental composition of all the samples across the different doping levels. The prominent peaks corresponding to La, Ni, and O, along with carbon, are observed, with no detectable peaks from other impurities. This observation aligns with the expected composition of PLNO, confirming the accurate composition of the sample. With a doping level of 10%, a clear peak for Ti is detected at a specific energy, corresponding to a weight percentage of 2.25%. Additionally, smaller peaks for La and Ni are present, with weight percentages of 47.05 and 15.76%, respectively. These outcomes further validate the exact composition of the LNO-II sample. The EDX spectrum at doping levels of

20% and 30% exhibits no additional elemental peaks, only showing the anticipated elements: La, Ni, O, C, and Ti. **Table 2** indicates that the precise composition of the prepared samples aligns with the stoichiometric ratios, confirming that the sample composition is optimal.

Braunauer–Emmett–Teller (BET) analysis is a highly recommended and efficient technique for revealing the textural characteristics, such as the availability of active sites from the SSA, pore size, and volume of synthesized samples through nitrogen ($N_2$) adsorption-desorption isotherms achieved at 77 K. The rationale behind choosing $N_2$ gas as an adsorbate for this purpose is its numerous features, such as inertness, cost-effectiveness, and superior sensitivity, which is particularly helpful in detecting small-sized pores. According to the recommended classification of isotherms by IUPAC, the isotherms obtained in the cases of PLNO and LNO-III, as depicted in **Figure 4**a,b, have been classified as type IV isotherms, indicating the mesoporous characteristics of PLNO and LNO-III-based materials. Furthermore, the low relative pressure ($P/P_o < 0.1$) region gives information regarding monolayer coverage of the concentration gradient of $N_2$ molecules to be readily adsorbed into small-sized pores readily available. In contrast, multilayer coverage occurs in a relative pressure region below 0.9, showcasing the layer-by-layer adsorption of $N_2$ gas molecules by subsequent layers due to van der Waals forces. Beyond this region, the next region is the plateau region, which highlights the saturation point where multilayer coverage appears at higher relative pressures ($P/P_o > 0.9$ to 1). In this context, Figure 4a,b, depicting the isotherms for PLNO and LNO-III, demonstrate an apparent upward shift due to an elevation in SSA attributed to the 30% MXene content compared to PLNO in the plateau region. The highest upward shift along the y-axis indicates the highest adsorbed quantity of $N_2$ gas compared to the others, due to the enhanced SSA.

The identical type IV hysteresis loops of PLNO and LNO-III often exhibit a hierarchical structure, yielding enhanced ionic conductivity, diffusion rate, and the highest contribution to anion mobility in PLNO, which improves when a 30% MXene content is added. This demonstrates an improvement in hierarchical porosity with interconnected channels, facilitating their ion transport properties. However, the diffusion pathways in PLNO are aggregated, which hinders ion transportation due to boosted diffusion resistance, as observed in the FESEM image displayed in Figure 3a.

In contrast, the differential pore volume versus pore radius in Figure 4b suggests that the dominant mesoporous networking is attributed to the 30% MXene concentration in PLNO, as shown in Figure 4b, which is supported by the comparison with PLNO in Figure 3d. More importantly, the ion transport features that yield

**Table 2.** Elemental composition of all samples.

| Sample | wt% La | wt% Ni | wt% O | wt% Ti | wt% C |
|---|---|---|---|---|---|
| PLNO | 56.57 | 23.89 | 19.54 | 0 | 2.34 |
| LNO-I | 47.05 | 15.76 | 22.84 | 2.25 | 12.36 |
| LNO-II | 43.18 | 15.30 | 24.81 | 4.20 | 17.97 |
| LNO-III | 39.09 | 14.04 | 26.53 | 6.09 | 13.34 |

**Batteries & Supercaps**

Research Article
doi.org/10.1002/batt.202500014

**Chemistry Europe**
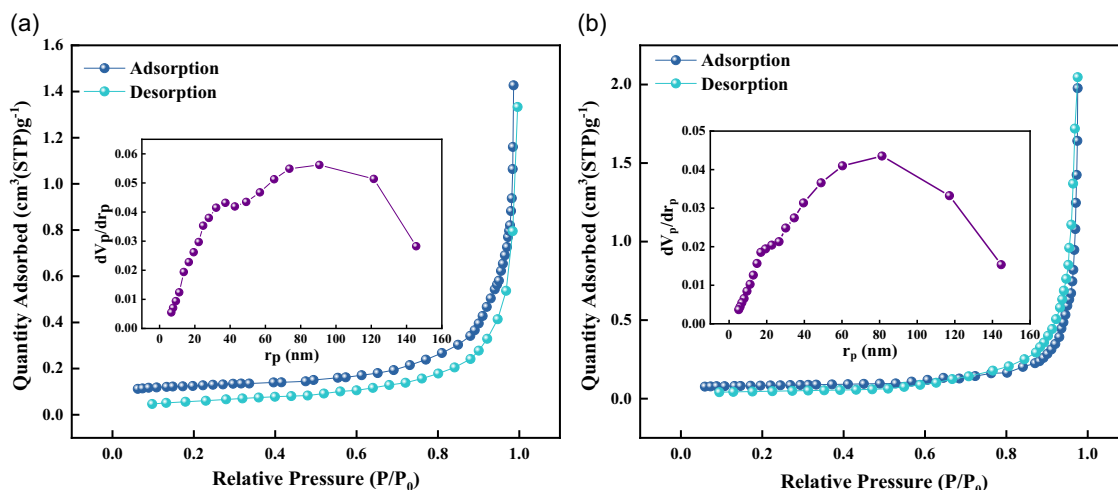European Chemical
Societies Publishing

**Figure 4.** a,b) Nitrogen adsorption-desorption isotherms of PLNO and LNO-III.

enhanced ionic conductivity, reduced ion resistance, and the highest contribution to anion mobility are crucial. Whereas hierarchical porosity is a combination of micro and mesoporous networks that commonly provides more conducting channels and facilitates ion transport. Such hierarchical porosity yields more active sites and is further enhanced with the addition of the highest MXene content to PLNO, causing variations in loop width and demonstrating a notable transition in the width of the hysteresis loop. These analyzes confirmed that LNO-III possessed fascinating textural characteristics, highlighting its potential as the best electrode material for SC applications.

CV is a widely used electrochemical analysis technique performed in potentiostat mode, providing insights into the reaction kinetics and electrochemical performance of synthesized samples. To enhance the analysis, the schematic setup of the three-electrode workstations is presented in Figure S4, Supporting Information. **Figure 5**a–d displays the voltammograms of PLNO, LNO-I, LNO-II, and LNO-III, attained at constant potential window ranging from 0–0.5 V to avoid decomposition of electrolytic species with the variety of scan rates (SRs) from 2.5–30 mV s$^{-1}$. In Figure 5a–d, the potential ranges of 0 to 0.33 V for PLNO, 0.31 V for LNO-I, 0.30 V for LNO-II, and 0.29 V for LNO-III suggest



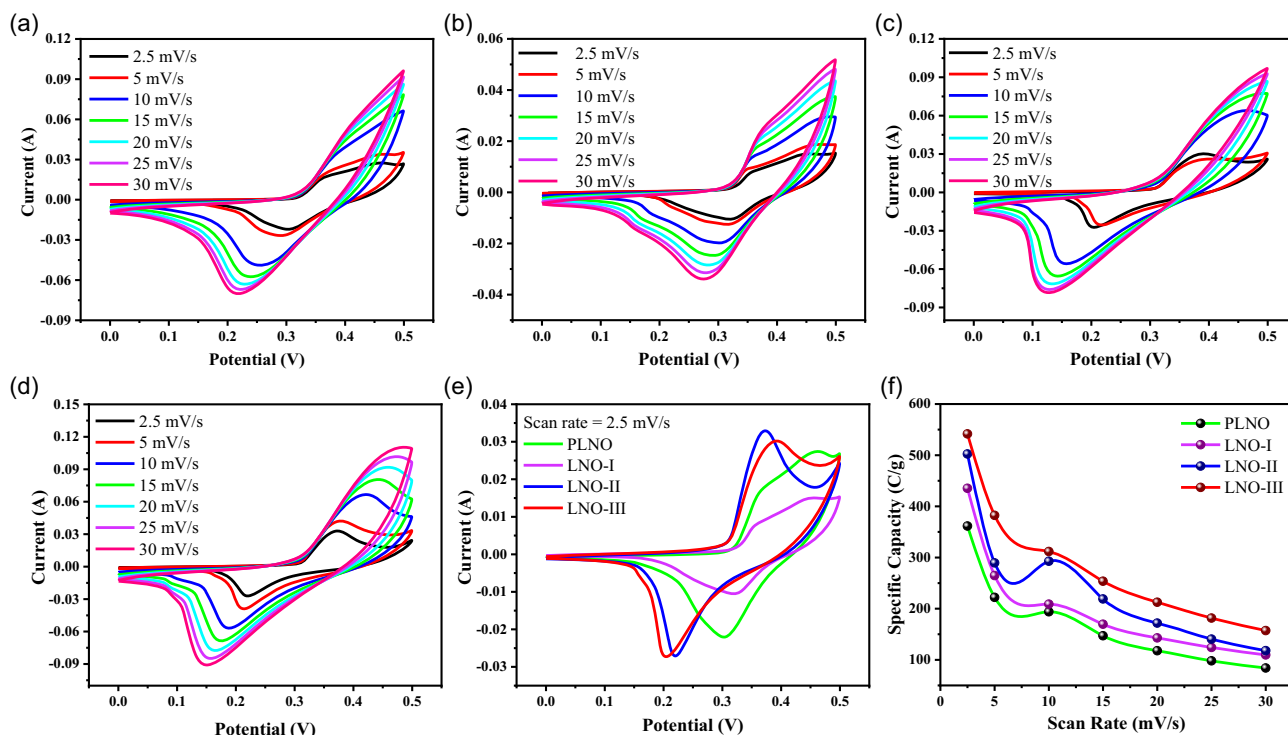**Figure 5.** CV curves at different SCs for a) PLNO, b) LNO-I, c) LNO-II, d) LNO-III, e) Comparison of all samples at 2.5 mV s$^{-1}$, and f) scan rate vs specific capacity.

**Batteries & Supercaps**

Research Article
doi.org/10.1002/batt.202500014

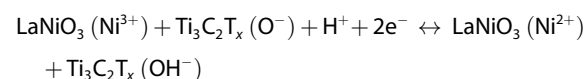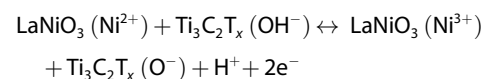**Chemistry Europe**
European Chemical
Societies Publishing

that these are the minimum potential ranges at which the prepared samples are activated, commonly known as background or equilibrium potentials. Figure 5a shows the voltammograms of PLNO, demonstrating a series of narrow intensity peaks even at higher SRs, indicating that the peak symmetry remains unchanged. This suggests that the PLNO system exhibits remarkable stability and durability, even under the influence of higher SRs. The only rationale behind this is an excellent contact between the electrode-electrolyte interfaces, suggesting that sufficient time is available for ions to migrate from the electrolyte to the electrode's tunnels. Similarly, LNO-I, LNO-II, and LNO-III followed the same trend; however, a noticeable projection in the hump has been observed in the case of LNO-I. The addition of 10% MXene appears to influence the material's characteristics, resulting in a progressively smoother texture as the MXene content increases to 20 and 30%. Including up to 30% MXene in the PLNO resulted in a broadening of the intensity peaks in the CV curves, indicating excellent conductivity. Consequently, the CV curves of LNO-III at 30% MXene content exhibited the optimal battery-type behavior, reflecting a substantial improvement in electrochemical performance.

In addition, at higher SRs, ions do not have sufficient time to penetrate the material's tunnels, which causes the narrowing of the intensity peaks in the CV curves. An increase in SR also influences the material's specific capacity, reaction kinetics, and behavior. The redox reaction peaks for PLNO, LNO-I, LNO-II, and LNO-III across all SRs were observed within extensively wider potential ranges of (0.33–0.46) V, (0.31–0.48) V, (0.30–0.0049) V, (0.29–0.50) V, and (0.20–0.30) V, (0.25–0.33) V, (0.15–0.25) V, and (0.10–0.20) V, for oxidation and reduction, respectively. This suggests that the peak shifts toward high and low potentials with increasing SR, indicating the excellent reversibility of these electrode materials. Obtained CV curves without significant distortion, which evidenced excellent contact between the electrode and the electrolyte interface. The CV curves in Figure 5a depicted the conversion of $Ni^{2+}$ to $Ni^{3+}$ in the case of PLNO, suggesting that a single electron participates in redox activity, as shown in the given chemical equation.[37]

$$LaNiO_3\,(Ni^{2+}) \leftrightarrow LaNiO_3\,(Ni^{3+}) + e^-$$

$$LaNiO_3\,(Ni^{3+}) + e^- \leftrightarrow LaNiO_3\,(Ni^{2+})$$
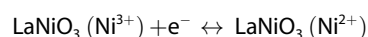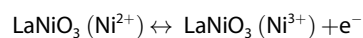
The CV curves presented in Figure 5b–d validate the redox activity of composites, including LNO-I, LNO-II, and LNO-III. The accompanying equations illustrate the electrochemical conversion mechanisms associated with these materials.

$$LaNiO_3\,(Ni^{2+}) + Ti_3C_2T_x\,(OH^-) \leftrightarrow LaNiO_3\,(Ni^{3+})$$
$$+ Ti_3C_2T_x\,(O^-) + H^+ + 2e^-$$

$$LaNiO_3\,(Ni^{3+}) + Ti_3C_2T_x\,(O^-) + H^+ + 2e^- \leftrightarrow LaNiO_3\,(Ni^{2+})$$
$$+ Ti_3C_2T_x\,(OH^-)$$

CV curves for different samples within specific potential ranges revealed information about the symmetry of the peaks, which is independent of SR, even at 30 mV s$^{-1}$. However, a slight

shift in the anodic peaks toward higher potentials and cathodic peaks toward lower potentials was attributed to fast ion transport. It was attributed to the synergistic effects of MXene content, which resulted in remarkable electrochemical efficiency. Figure 5e indicates that LNO-II and LNO-III exhibit more pronounced capacitive behavior than PLNO and LNO-I, as plotted at the lowest SR of 2.5 mV s$^{-1}$. Furthermore, at this SR, due to the excessive number of active sites provided by MXene, which is attributed to its unique layered structure, it offers ease for ions that can easily penetrate the material's tunnels. Such attributions favor efficient charge transfer mechanisms. However, more time is available for ions to contribute to the redox activity, resulting in the duck-like shapes of CV curves and the development of a slight double-layer capacitance. The specific capacities ($Q_s$) of synthesized samples have been computed using Equation (3).

$$Q_s = \frac{\int_{V_i}^{V_f} I\,dV}{mv} \tag{3}$$

Herein, $Q_s$ represents the specific capacity, and the integral part reflects the area under the CV curve, while $m$ and $v$ denote the active mass and specific resistance, respectively. Figure 5f shows the trend of SR versus $Q_s$ measured from CV curves for PLNO, LNO-I, LNO-II, and LNO-III at different SRs, ranging from 2.5 to 30 mV s$^{-1}$, as reported in **Table 3**. To further comprehend the quantitative analysis of the samples, Figure S5, Supporting Information, is provided to illustrate how the concentration of MXene affects the electrode material's capacity at 2.5 mV s$^{-1}$. Here, it can be observed that the LNO-III-based electrode exhibits an excellent $Q_s$ of ≈541.60 C g$^{-1}$, which is the highest among the others.

To compare the experimental and theoretical capacities, we calculated the theoretical capacity for LNO. As the theoretical capacity is a pivotal concept in electrochemistry, it quantifies the maximum amount of electrical charge that can be stored in a material under ideal conditions in an electrochemical cell. This charge is primarily determined by the charge carriers, such as ions and electrons, involved in electrochemical activity. Theoretical capacity can be determined by utilizing Faraday's law, which relates the total amount of charge transferred during the reaction to the amount of substance that undergoes the electrochemical change. This relationship is expressed in Equation (4).

**Table 3.** Specific capacities of PLNO, LNO-I, LNO-II, and LNO-III electrodes at different SCs.

| SCs [V s$^{-1}$] | PLNO | LNO-I | LNO-II | LNO-III |
|---|---|---|---|---|
| | Specific capacities [C g$^{-1}$] | | | |
| 0.0025 | 361.51 | 435.40 | 502.40 | 541.60 |
| 0.005 | 222.13 | 264.80 | 289.50 | 382.40 |
| 0.010 | 193.97 | 208.95 | 292.80 | 311.80 |
| 0.015 | 147.05 | 169.63 | 219.06 | 253.73 |
| 0.020 | 117.83 | 142.97 | 171.80 | 212.60 |
| 0.025 | 98.06 | 124.18 | 140.64 | 181.60 |
| 0.030 | 84.10 | 109.66 | 118.01 | 157.20 |

**Batteries & Supercaps**

Research Article
doi.org/10.1002/batt.202500014

**Chemistry Europe**
European Chemical
Societies Publishing

$$Q_{\text{Theoretical}} = \frac{n \times F}{M_{\text{w}}} \tag{4}$$

From this formula, the theoretical capacity of LNO using the values of parameters like $F = 96{,}485\ \text{C mol}^{-1}$ (Faraday's constant), $n = 1$ (the number of electrons involved in the reaction), and $M_{\text{w}} = 213.60\ \text{g mol}^{-1}$ (the molar mass of $\text{LaNiO}_3$) is calculated to be $451.8\ \text{C g}^{-1}$.

It's essential to note that the experimental capacity is typically less than the calculated capacity due to electrochemical limitations, particularly when the host material traps the charge carriers, such as $K^+$ ions. This discrepancy between theoretical and experimental capacity highlights the practical challenges in achieving a material's full potential in an electrochemical cell. The lack of availability of these charge carriers trapped in the material lattices limits the charge storage capacity. The partial extraction of charge carriers from the lattices of the host material is the reason behind the gap between practical capacity and theoretical capacity.

To analyze the behavior of the prepared electrodes more deeply, a theoretical approach was employed to explain how charge storage mechanisms were incorporated into PLNO, LNO-I, LNO-II, and LNO-III. Anodic and cathodic peaks shifting toward higher and lower potentials, respectively, are expected to arise from the transitions of two distinct mechanisms: pseudocapacitive and EDLC, which contribute to the overall capacitance. For this purpose, Cottrell's equation was quantified into Equation (5).

$$i_{\text{peak}} = av^b \text{ or } \log(i_{\text{peak}}) = b\log(v) + \log(a) \tag{5}$$

Herein, $i_{\text{peak}}$ indicates the anodic and cathodic peak currents, whereas $a$ and $b$ are adjustable parameters and $v$ refers to the SR. The value of $b$ is crucial in determining the electrochemical behavior of a material. It refers to the slope value quantified from

the linear fitting of $\log v$ versus $\log i$, indicating the material's behavior. When $b \approx 1$, it suggests the dominance of the capacitive contribution, which represents the capacitive behavior of a material associated with non Faradaic processes. While $b \approx 0.5$ indicates the diffusion-controlled mechanism belonging to Faradaic processes. If its value lies between 1 and 0.5 or below 0.5, it will indicate hybrid behavior (battery type). The average $b$-value results obtained from linear fitting are 0.27, 0.39, 0.61, and 0.79 for PLNO, LNO-I, LNO-II, and LNO-III, respectively, suggesting hybrid behaviors. Such behaviors describe the occurrences of faradaic and nonfaradaic processes, which we have observed in **Figure 6**a–d. The combined $b$-value graph is also displayed in Figure S10, Supporting Information, indicating different regions. Dunn et al., proposed the Dunn method to attain a deeper insight into the charge storage mechanisms to calculate the material's capacitive and diffusive-controlled contributions within the device. They proposed a relationship that describes the combination of capacitive and diffusion-controlled currents, depending on the SR, and quantified it in Equation (8).

$$i = i_{\text{c}} + i_{\text{D}} \tag{6}$$

$$i_{\text{peak}} = k_1 v + k_2 v^{0.5} \tag{7}$$

Or

$$\frac{i_{\text{peak}}}{v^{0.5}} = k_1 v^{0.5} + k_2 \tag{8}$$

Equation (8) illustrates the linear relationship between $k_1 v$ and $k_2 v^{0.5}$ at a specific SR, corresponding to capacitive and diffusive current contributions, respectively.[37,38] While $k_1$ and $k_2$ are constants, which reflect the slopes and intercepts and are computed from the linear fitting of $v^{0.5}$ to $\frac{i_{\text{peak}}}{v^{0.5}}$ ratios, which are demonstrated in Figure 6e–h, contribute to overall capacitance. Likewise,
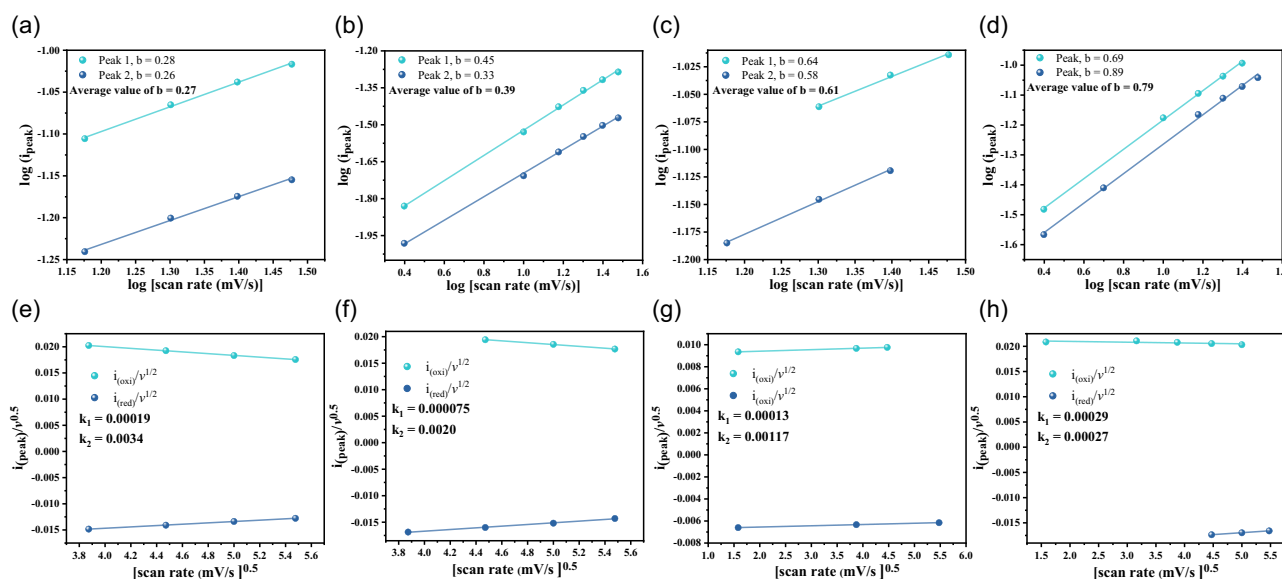


**Figure 6.** a–d) Values of b (slopes) calculated from the CV curves upon linear fitting, and e–h) values of $k_1$ and $k_2$ for PLNO, LNO-I, LNO-II, and LNO-III, respectively.

**Batteries & Supercaps**

Research Article
doi.org/10.1002/batt.202500014

**Chemistry Europe**
European Chemical
Societies Publishing

Figure 7a–d depicts the graphs of contribution ratios for capacitive and diffusion-controlled processes at various SRs for PLNO, LNO-I, LNO-II, and LNO-III. The decrease in diffusion-controlled processes attributed to faradaic processes indicates a shortening of the diffusion distance and less time available for ions to diffuse, as well as limiting the intercalation of ions due to the limited availability of active sites at higher SRs **Table 4**. It can be seen from Figure 7a–d that an increase in SR causes a rise in capacitive contributions belonging to surface mechanisms, which rationalizes the shorting of redox activities, encouraging the capacitor-like behavior at higher SRs due to elevated nonFaradaic processes.[39–44] Conclusively, theoretical predictions confirm the superior electrochemical behavior of LNO-III and suggest it as a potential candidate for electrode material in SC applications. Figure S6–S9, Supporting Information, illustrates the capacitive and diffusive contributions at each SR.

For comprehensive electrochemical analysis, GCD analysis was performed to assess how an electrode stores charges while the electrochemical analyzer is in galvanostatic mode. GCD tests maintained the potential window range from 0 to 0.5 V at various current densities, including ≈2.5, 5, 7.5, and 10 A g$^{-1}$. **Figure 8**a–d presents the GCD curves for the fabricated electrodes, including PLNO, LNO-I, LNO-II, and LNO-III. These curves indicate a relationship with redox reactions, as observed in the CV analysis, which exhibits characteristics consistent with those of a battery. As mentioned, each GCD profile displayed notable symmetry, indicating smooth charge storage mechanisms that favor excellent electrochemical performance. It can also be observed that a pronounced elevation in the area under the GCD curves leads to a significant increase in $Q_s$.
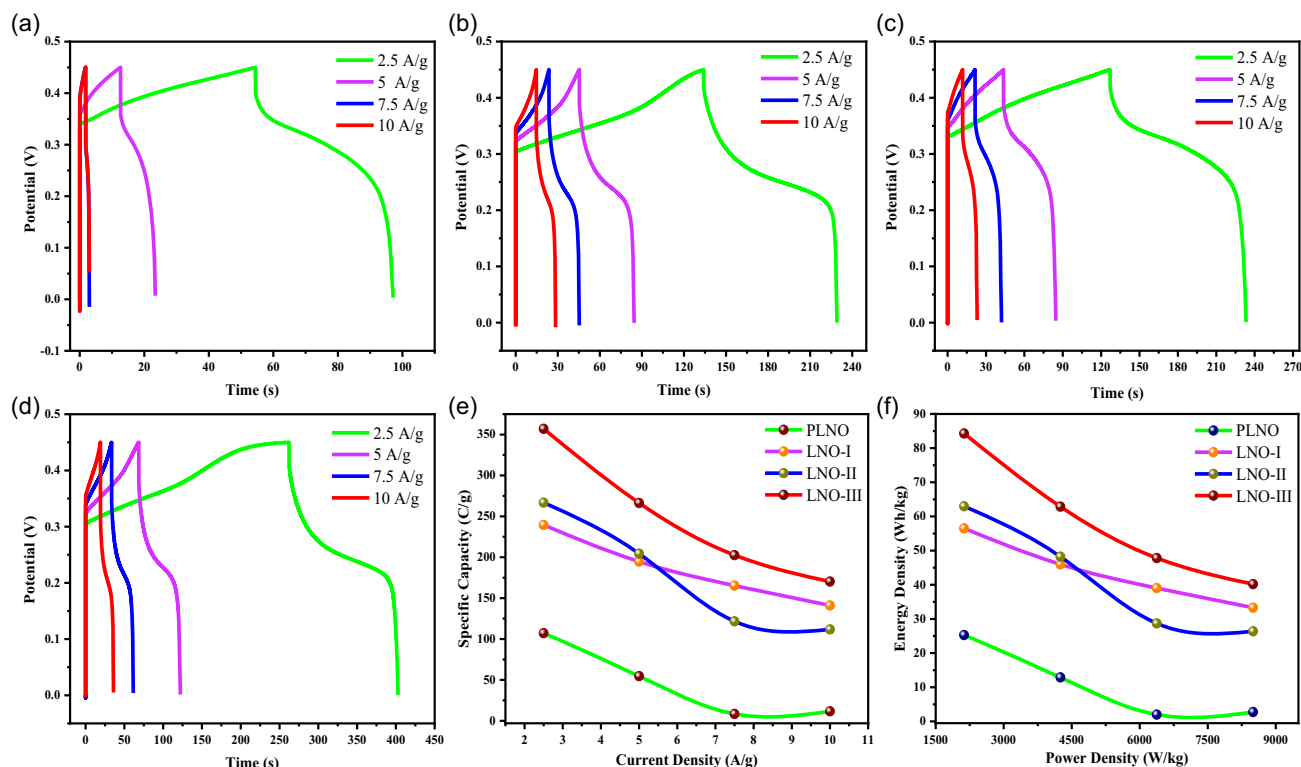
**Table 4.** Specific capacity, energy density, and power density of PLNO, LNO-I, LNO-II, and LNO-III.

| Sample | Current density [A g$^{-1}$] | Discharge time [s] | Specific capacity [C g$^{-1}$] | Energy density [Wh kg$^{-1}$] | Power density [W kg$^{-1}$] |
|---|---|---|---|---|---|
| PLNO | 2.5 | 42.85 | 107.12 | 25.29 | 2125 |
| | 5 | 10.92 | 54.60 | 12.89 | 4250 |
| | 7.5 | 1.13 | 8.47 | 2.01 | 6375 |
| | 10 | 1.17 | 11.70 | 2.76 | 8500 |
| LNO-I | 2.5 | 95.79 | 239.48 | 56.54 | 2125 |
| | 5 | 38.94 | 194.70 | 45.97 | 4250 |
| | 7.5 | 22.05 | 165.37 | 39.04 | 6375 |
| | 10 | 14.11 | 141.10 | 33.31 | 8500 |
| LNO-II | 2.5 | 106.70 | 266.75 | 62.98 | 2125 |
| | 5 | 40.87 | 204.35 | 48.24 | 4250 |
| | 7.5 | 16.21 | 121.57 | 28.70 | 6375 |
| | 10 | 11.18 | 111.80 | 26.39 | 8500 |
| LNO-III | 2.5 | 142.82 | 357.05 | 84.30 | 2125 |
| | 5 | 53.26 | 266.30 | 62.87 | 4250 |
| | 7.5 | 27.01 | 202.57 | 47.83 | 6375 |
| | 10 | 17.03 | 170.30 | 40.20 | 8500 |

It can also be inferred that adding MXene content has led to an increase in discharge time due to enhanced ionic conductivity, increased ion mobility, and reduced resistance associated with the potential drop, which causes the polarization effects as observed in Figure 8a–d and tabulated in Table 4. Such a trend
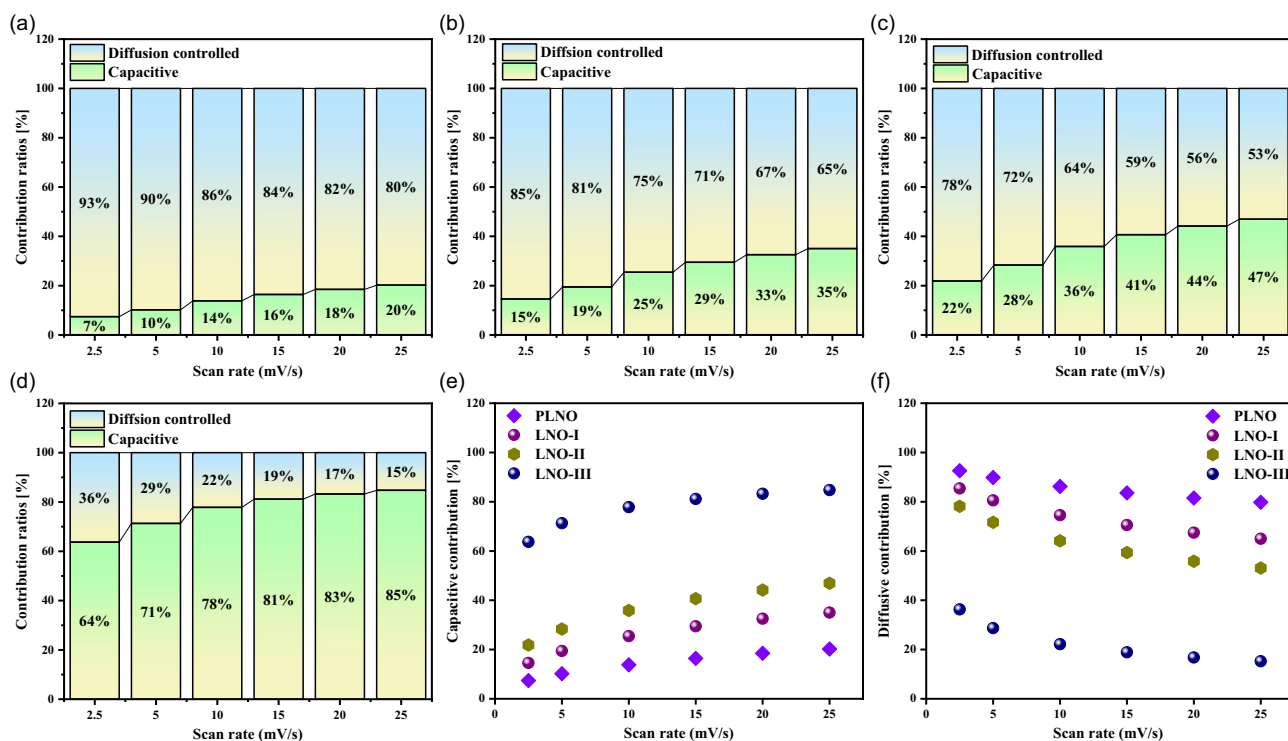


**Figure 7.** a–d) Ratios of capacitive and diffusive controlled process, e) capacitive versus scan rate, and f) diffusive versus scan rate, for PLNO, LNO-I, LNO-II, and LNO-III, respectively.

**Batteries & Supercaps**

Research Article
doi.org/10.1002/batt.202500014

**Chemistry Europe**
European Chemical
Societies Publishing

**Figure 8.** a–d) GCD curves at different current densities for PLNO, LNO-I, LNO-II, and LNO-III, e) current density vs specific capacities, and f) power densities vs energy densities.

is suppressed as the current density increases because there is less time available for ions to be stored for a prolonged period. This has led to a reduced charge storage capability of the electrode material, which is improved with an increase in MXene concentration. Based on these analyzes, LNO-III exhibited an outstanding discharge rate compared to others due to its excellent conductivity and active sites, which are attributed to the highest MXene content. GCD profiles indicated that an increase in current density results in shorter charging and discharging time durations, suggesting fast-rate reaction kinetics. Additionally, Figure 8e reflects the correlation between current density versus $Q_s$ for PLNO and PLNO/MXene. It was observed that as the current density increases, all samples discharge rapidly, underscoring the importance of how effectively ions diffuse into the material and suppress the capacity. At lower current densities, excessive amounts of ions are available for absorption into the inner layers of materials, as more time is available compared to higher current densities. Adding MXene content improves conductivity and response to current. Conclusively, 30% MXene addition content exhibited the highest $Q_s$ among all others. The values of $Q_s$ at specified current densities for all samples were calculated by applying Equation (9) below.

$$Q_s = I_m \times \Delta t \qquad (9)$$

Here, $I_m$ reflects the current density, and $\Delta t$ represents the discharging time, which is used to calculate $Q_s$ and to understand how it affects the given parameters and the variation in MXene content. The highest value of $Q_s$ from the above equation was

observed to be about 357.05 C g⁻¹ attributed to LNO-III. It can be seen that the higher concentration of MXene content exhibited the elevation in $Q_s$. The following equations have also been adopted to compute the ED and PD values for PLNO and PLNO/MXene composites.

$$ED\left(\frac{Wh}{kg}\right) = \frac{\Delta V \times Q_s}{2 \times 3.6} \qquad (10)$$

$$PD\left(\frac{W}{kg}\right) = \frac{ED \times 3600}{\Delta t} \qquad (11)$$

Using the above equations, the values of ED and PD for prepared samples have been computed as reported in Table 3. Notably, the remarkable ED value at 2.5 A g⁻¹ was 84.87 Wh kg⁻¹ for LNO-III. An outstanding PD of 8,500 W kg⁻¹ at 10 A g⁻¹ was also obtained and compared with previously reported data from researchers, as tabulated in **Table 5**.[31,32,34–50] In this context, Figure 8f displays the Ragone plot, suggesting a correlation between ED and PD, where it can be observed that an increase in PD results in a decrease in ED, as the stored ions are less available for transfer.

It's important to evaluate the lifespan of the electrode material. A stability test is crucial to highlight its potential for use in high-performance SC technology. A cyclic stability test of an optimized sample (LNO-III) was conducted for 10 000 continuous charging and discharging cycles, demonstrating an excellent performance of ≈88.12%. This exceptional result highlights the significant potential of the electrode material. The capability of

**Batteries & Supercaps**

Research Article
doi.org/10.1002/batt.202500014

**Chemistry Europe**
European Chemical
Societies Publishing

**Table 5.** Values of elements for the corresponding fit circuit. $R_1 = R_s$, $R_2 = R_{ct}$, $C_1 =$ Capacitance, $Q_1, Q_2 =$ constant phase elements, and $W_1 =$ Warburg impedance.

| Sample | $R_1$ [Ω] | $R_2$ [Ω] | $C_1$ [F] | $Q_1$ [Fs$^{(a-1)}$] | $Q_2$ [Fs$^{(a-1)}$] | $W_1$ [Ωs$^{-1/2}$] |
|---|---|---|---|---|---|---|
| PLNO | 0.94 | 7.07 | 0.004 | 0.018 | 0.17 | 3.06 |
| LNO-I | 1.05 | 4.07 | 0.61 | 0.009 | 2.85 | 2.16 |
| LNO-II | 0.89 | 2.47 | 0.15 | 0.006 | 3.55 | 1.03 |
| LNO-III | 1.01 | 0.84 | 2.17 | 0.303 | 0.61 | 0.88 |

effectively delivering the stored charge, commonly referred to as Coulombic efficiency, was calculated to be 97.82%, as shown in **Figure 9**. It can be inferred that such an outstanding performance is primarily attributed to the 30% MXene integration into the LNO-based electrode material, compared to other as-synthesized samples. So, the LNO-III is a potential candidate for advanced energy storage devices.

A series of EIS tests was conducted to analyze the reaction kinetics and electrochemical response of the fabricated electrodes, aiming to determine resistive components, including solution resistance ($R_s$), charge transfer resistance ($R_{ct}$), and Warburg impedance (W). All these parameters have been acquired within a limited frequency range starting from $10^{-2}$–$10^5$ Hz. In this regard, **Figure 10**a is displayed, showcasing the Nyquist plots for the prepared samples plotted against the real and imaginary parts of impedance, providing deeper insight into reaction kinetics. It is obvious how resistive and capacitive components vary. The Nyquist plots have been configured into three fundamentals. First, the high-frequency region indicates the series resistance associated with solution resistance. The second one highlights the intermediate frequency region and depicts the charge transfer resistance. The diameter of the semicircle in EIS spectra provides insight into the charge transfer resistance associated with the electrode-electrolyte interface.

It can be observed from Figure 10a that the inclusion of 10, 20, and 30% MXene content causes the suppression of the resistive component and reduces the diameter of the semicircle sequence-wise, suggesting an increase in conductivity.
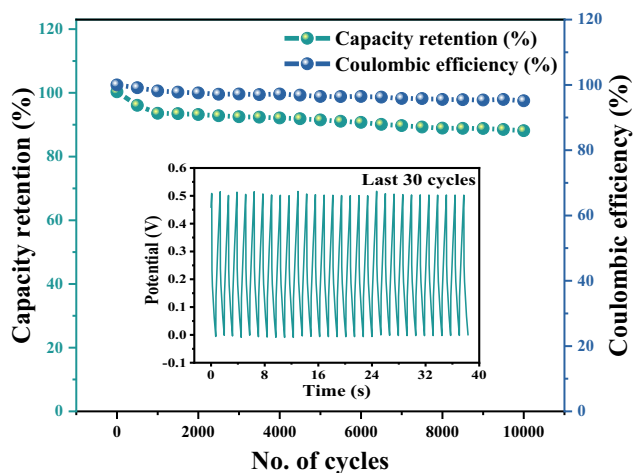


**Figure 9.** Cyclic stability of LNO-III based electrode at 1 mA.

Moreover, the straight line immediately following the semicircle illustrates the diffusion process and Warburg resistance, which are associated with the charge transfer resistance. The line slope deflected toward the y-axis, suggesting that capacitive processes are predominant and ions are rapidly diffused. Figure 10b–e shows the impedance spectra of all samples acquired after curve fitting using Biologic EC lab V11.60 software and their Randle circuits. EIS curve fitting parameters have been tabulated in Table 5, from which it can be evaluated that LNO-III demonstrated an extremely low $R_{ct}$ value of ≈0.84 Ω, compared to the others (7.07, 4.07, and 2.47 Ω for PLNO, LNO-I, and LNO-II, respectively). It can be concluded from Figure 7e and **Table 6** that LNO-III exhibits exceptional conductivity, as evidenced by a small arc semicircle, indicating the successful incorporation of MXene content into PLNO and making it a potential candidate among others.

A Bode plot determines the relaxation time that ions usually take to attain equilibrium after absorbing energy. For this purpose, Figure 10f depicts the Bode plot, which represents the frequency-phase relationship, demonstrating how the frequency variation in the material is associated with a shift in the phase angle Table 5. The impedance characteristics of SC fluctuate between pure capacitive ($\theta = 90°$) in low-frequency regions and resistive ($\theta = 0°$) in high-frequency areas. In comparison, at a knee frequency ($\theta = 45°$), both impedances contribute equally, defining the material's electrochemical response in these regions. Moreover, the relaxation time constant ($\tau_0 = 1/2\pi f_c$) defined by the time a device takes to discharge the stored energy was calculated from the frequency-phase Bode plot to evaluate the device's efficiency, listed in Table 5. A lower $\tau_0$ of ≈17 ms for LNO-III suggests a higher rate capability due to the small internal resistance, resulting in the rapid diffusion of ions compared to PLNO, LNO-I, and LNO-II.

Knowing the diffusion coefficient values of synthesized samples, one can infer that they play a crucial role in predicting electrochemical performance. Therefore, a theoretical approach has been developed to accurately compute the rate of ion diffusion from the electrolyte to the electrode surface, thereby enhancing our understanding of system behavior and efficiency. A higher diffusion coefficient indicates enhanced electrochemical efficiency, characterized by rapid ion transportation. This acceleration facilitates efficient redox reactions at the electrode surface and is crucial for applications such as batteries and SCs. In this context, using KOH as an electrolyte, the diffusion coefficient values ($D_K^{+1}$) for prepared samples have been determined using Equation (12).

$$D^{EIS}/K^+ = \frac{R^2 T^2}{2 \times A^2 \times n^4 \times F^4 \times c^2 \times \delta^2} \tag{12}$$

Herein, $D^{EIS}/K^+$ represents the diffusion coefficient determined from EIS data using KOH electrolyte. R, T, and F denote the universal gas constant (8.314 mol$^{-1}$ K$^{-1}$), room temperature (RT) (298 K), and Faraday's constant (96 485 C mol$^{-1}$), respectively.[51] While parameters A, n, δ, and c are associated with the surface area of the electrode taken as 0.5 cm$^2$, the number of electrons participating in redox activity, the Warburg coefficient determined from the slope of linear fitting of $\omega^{-1/2}$ versus
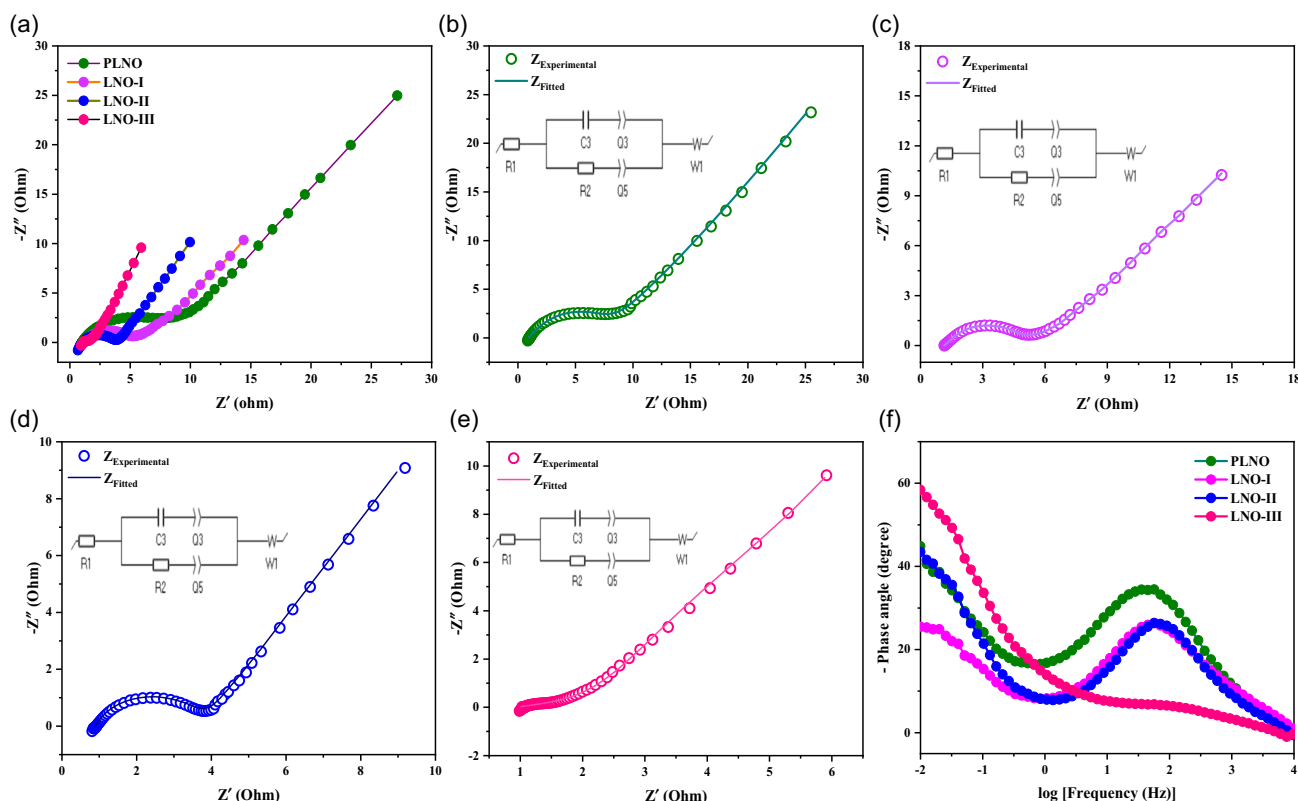
**Figure 10.** a) Combined EIS spectra, b–e) EIS curve fitting spectra with appropriate Randle circuit using EC Lab Software, and f) Bode plot for all fabricated electrodes.

**Table 6.** Comparison of electrochemical performance parameters of different related materials.

| Sample | Specific capacitance [F g$^{-1}$] | Energy density [Wh kg$^{-1}$] | Power density [W kg$^{-1}$] | Cyclability [%] | References |
|---|---|---|---|---|---|
| Nd-doped LaNiO$_3$ | 64.38 | 20.92 | 846.56 | – | [34] |
| LaNiO$_3$/NiO | 326.78 | 30.4 | 1800 | 97.7% after 3 k cycles | [45] |
| Ti$_3$C$_2$T$_x$/NiCoO$_3$ | 1025 | 36.67 | 800 | 88.2% after 5 k cycles | [32] |
| Ti$_3$C$_2$T$_x$/PANI | 430 | 38 | 808 | 84% after 10 k cycles | [31] |
| Ti$_3$C$_2$T$_x$/ZrO$_2$ NC | 483.6 | 75.60 | 1145 | 88.85% after 5 k cycles | [46] |
| Fe substituted-SrCoO$_3$ | 1035.9 | 26.2 | 800 | 85.71% after 5 k cycles | [47] |
| SrSnO$_3$/rGO | 1385 | 66 | 293 | 86% after 5 k cycles | [48] |
| BaCeO$_3$@rGO | 1488 | 65 | 324 | 90% after 5 k cycles | [49] |
| Mn doped BiFeO$_3$ | 1795 | 41.91 | 205 | 90% after 5 k cycles | [50] |
| LNO-III | 541.60 C g$^{-1}$ | 84.87 | 8500 | 88.12% after 10 k cycles | This work |

$Z'$ as depicted in Figure S11, Supporting Information, and concentration of electrolytic species at the electrode surface computed from Nernst equation as standardized in Equation (13).

$$E = E^0 + \frac{RT}{nF} ln \frac{C_{surface}}{C_{bulk}} \tag{13}$$

The Nernst equation can be generalized into Equation (14)

$$C_{surface} = C_{bulk} \times e^{\left(\frac{nF(E-E^\circ)}{RT}\right)} \tag{14}$$

Here, $C_{surface}$ reflects the concentration of electrolytes at the electrode surface, $C_{bulk}$ indicates the total concentration of

electrolytes, and $E - E^\circ$ indicates the difference between the applied potential and the standard potential. While $n$ represents the number of electrons transferred, $F$ is Faraday's constant, and $R$ and $T$ are the universal gas constant and the temperature, respectively.[52,53] **Table 7** reports the values calculated from the diffusion coefficient. LNO-III exhibits an impressive diffusion coefficient of $\approx 9.5 \times 10^{-13}$ m s$^{-2}$, indicating exceptional ease of ion transport.

Ionic conductivity refers to the extent to which an electrode material undergoes redox activity, which is crucial in determining the material's electrochemical performance in SC technology. Higher ionic conductivity enables impressive ion transportation

**Table 7.** Parameters obtained from EIS measurements of PLNO, LNO-I, LNO-II, and LNO-III.

| Sample | $\tau_0$ [ms] | $\delta$ [$\Omega s^{-1/2}$] | $D_K^{+1}$ [$m^2 s^{-1}$] | $\sigma$ [S cm$^{-1}$] | $t_+$ |
|---|---|---|---|---|---|
| PLNO | 100 | 5.84 | $2.45 \times 10^{-14}$ | $5.6 \times 10^{-3}$ | 0.94 |
| LNO-I | 90 | 2.89 | $4.96 \times 10^{-14}$ | $5.9 \times 10^{-3}$ | 0.53 |
| LNO-II | 85 | 1.65 | $8.69 \times 10^{-14}$ | $6.0 \times 10^{-3}$ | 0.46 |
| LNO-III | 17 | 0.15 | $9.5 \times 10^{-13}$ | $6.3 \times 10^{-3}$ | 0.32 |

and enhances the redox reactions, resulting in a more efficient charge storage mechanism. To attain its precise measurements, ionic conductivity is quantified into Equation (15).

$$\sigma = \frac{L}{R_i \times A} \tag{15}$$

Here, $R_i$ represents the ionic resistance associated with solution resistance ($R_s$), while $\sigma$, $L$, and $A$ stand for ionic conductivity, electrode thickness, and electrode surface area, respectively.[54,55] It is evident from Table 7 that LNO-III inherits an excellent ionic conductivity of about $6.3 \times 10^{-3}$ S cm$^{-1}$ as compared to PLNO ($5.6 \times 10^{-3}$ S cm$^{-1}$), LNO-I ($5.9 \times 10^{-3}$ S cm$^{-1}$), and LN-II ($6.0 \times 10^{-3}$ S cm$^{-1}$). Additionally, Figure S12, Supporting Information, has been presented to demonstrate the ionic conductivity of all samples.

The transference number defines the fractions of total current driven by cations and anions, contributing to the overall current within the device. It's a fact that not all ions in the electrolyte contribute equally to ionic conduction, depending on several factors, such as the small-sized ions generally giving rise to higher mobilities, the polarization effect, defects, and temperature, among others. In brief, the transference number indicates the likelihood of ions contributing to the overall current, ranging from 0 to 1.[56] In this context, Equation (16), proposed by Sorenson & Jacobsen

$$t_+ = \frac{1}{1 + Z_d(0)/R_b} \tag{16}$$

In the above equation, $t_+$ stands for transference number cations; conversely, $Z_d(0)$ represents the Warburg impedance in low-frequency regions, while $R_b$ reflects the electrolyte resistance.[57,58] The transference number of cations enables us to determine it for anions because it is the sum of both contributions. In our experiment, the transference numbers for cations in the cases of PLNO, LNO-I, LNO-II, and LNO-III were observed to be 0.94, 0.53, 0.46, and 0.32, respectively, as determined from the equation as mentioned earlier. It can be inferred that the inclusion of MXene resulted in a suppression of the cation transference number, which is consistent with the rationale behind the increase in the anion transference number. Hence, it can be concluded that the LNO-III-based electrode exhibits elevated anion mobility, contributing to the overall current as tabulated in Table 7.

## 4. Conclusion

In conclusion, we have synthesized LaNiO$_3$ (PLNO) using the hydrothermal route. This was then successfully incorporated with 0, 10, 20, and 30% MXene through the solvothermal method and labeled as PLNO, LNO-I, LNO-II, and LNO-III to prepare the electrode material for supercapacitors. In this context, techniques such as XRD, SEM, EDX, and BET were employed to confirm the crystalline nature, unique combinations of morphologies, ensure the absence of impurities, and verify the meso- and macroporous nature. On an electrochemical survey using a three-electrode assembly, an outstanding specific capacity of $\approx$541.60 mAh g$^{-1}$ at 2.5 mV s$^{-1}$ was observed from the LNO-III-based electrode material, while demonstrating an impressive energy density of $\approx$84.89 Wh kg$^{-1}$, along with an outstanding power density of 8500 W kg$^{-1}$. Moreover, the exceptional cyclic stability of 88.12% has been demonstrated by the LNO-III electrode material with improved ion transport properties, a high diffusion rate ($9.5 \times 10^{-13}$ m$^2$ s$^{-1}$), good ionic conductivity ($6.3 \times 10^{-3}$ S cm$^{-1}$), and a transference number ($t_+$) of 0.3, suggesting its remarkable potential for advanced supercapacitor applications.

## Conflict of Interest

The authors declare no conflict of interest.

## Data Availability Statement

The data that support the findings of this study are available from the corresponding author upon reasonable request.

[1] J. Li, Y. Li, H. Liu, F. Ran, *Nano Energy* **2024**, *128*, 109839.
[2] J. Theerthagiri, K. Karuppasamy, A. Min, D. Govindarajan, M. L. Kumari, G. Muthusamy, S. Kheawhom, H.-S. Kim, M. Y. Choi, *Appl. Phys. Rev.* **2022**, *9* 041314.
[3] X. Zhang, M. S. Javed, S. Ali, A. Ahmad, S. S. A. Shah, I. Hussain, D. Choi, A. M. Tighezza, C. Tag-Eldin, C. Xia, *Nano Energy* **2024**, *120*, 109108.
[4] Y. Li, R. Ding, *Nano Energy* **2024**, *124*, 109430.
[5] H. Lee, J. Theerthagiri, M. A. Kumari, A. Min, C. J. Moon, V. Anbazhagan, R. L. Brutchey, M. Y. Choi, *Int. J. Hydrogen Energy* **2024**, *57*, 176.
[6] Y. Jeong, S. S. Naik, J. Theerthagiri, C. J. Moon, A. Min, M. A. Kumari, M. Y. Choi, *Chem. Eng. J.* **2023**, *470*, 144034.
[7] J. He, L. Cao, J. Cui, G. Fu, R. Jiang, X. Xu, C. Guan, *Adv. Mater.* **2024**, *36*, 2306090.
[8] S. J. Lee, J. Theerthagiri, P. Nithyadharseni, P. Arunachalam, D. Balaji, A. M. Kumar, J. Madhavan, V. Mittal, M. Y. Choi, *Renewable Sustainable Energy Rev.* **2021**, *143*, 110849.

[9] X. Zheng, C. Han, C. Lee, W. Yao, C. Zhi, Y. Tang, *Prog. Mater. Sci.* **2024**, *143*, 101253.

[10] K. Narthana, G. Durai, P. Kuppusami, J. Theerthagiri, S. Sujatha, S. J. Lee, M. Y. Choi, *Int. J. Energy Res.* **2021**, *45*, 9983.

[11] Y. Wang, T. Xu, K. Liu, M. Zhang, X. Cai, C. Si, *Aggregate* **2024**, *5*, e428.

[12] M. A. Aziz, S. S. Shah, *Biomass-Based Supercapacitors: Design, Fabrication and Sustainability*, John Wiley & Sons **2023**.

[13] A. Ray, A. Roy, M. Ghosh, J. A. Ramos-Ramón, S. Saha, U. Pal, S. K. Bhattacharya, S. Das, *Appl. Surf. Sci.* **2019**, *463*, 513.

[14] A. Patra, K. Namsheer, J. R. Jose, S. Sahoo, B. Chakraborty, C. S. Rout, *J. Mater. Chem. A* **2021**, *9*, 25852.

[15] F. Bibi, O. Gerard, A. J. Khan, M. Khalid, A. Numan, *Categories of Pseudocapacitor: Intrinsic, Extrinsic, and Intercalation Materials, in Supercapacitors*, Elsevier **2024**, pp. 45–70.

[16] M. Saleem, F. Ahmad, M. Fatima, A. Shahzad, M. S. Javed, S. Atiq, M. A. Khan, M. Danish, O. Munir, S. M. Bin Arif, *J. Energy Storage* **2024**, *76*, 109822.

[17] B. Anasori, Ü. G. Gogotsi, *2D Metal Carbides and Nitrides (MXenes)*, Springer **2019**.

[18] A. Abdisattar, M. Yeleuov, C. Daulbayev, K. Askaruly, A. Tolynbekov, A. Taurbekov, N. Prikhodko, *Electrochem. Commun.* **2022**, *142*, 107373.

[19] Q. Zhang, R. Fan, W. Cheng, P. Ji, J. Sheng, Q. Liao, H. Lai, X. Fu, C. Zhang, H. Li, *Adv. Sci.* **2022**, *9*, 2202748.

[20] M. Alhabeb, K. Maleski, B. Anasori, P. Lelyukh, L. Clark, S. Sin, Y. Gogotsi, *Chem. Mater.* **2017**, *29*, 7633.

[21] H. Kim, C. Lim, J. Gu, H. Y. Jeong, J. W. Han, J. H. Jang, Y. Bu, *Adv. Energy Mater.* **2024**, *14*, 2401307.

[22] Z. A. Sheikh, D. Vikraman, H. Kim, S. Aftab, S. F. Shaikh, F. Shahzad, J. Jung, H.-S. Kim, S. Hussain, D.-K. Kim, *J. Energy Storage* **2024**, *81*, 110342.

[23] S. Yetiman, H. Peçenek, F. K. Dokan, S. Sanduvaç, M. Serdar Onses, E. Yılmaz, E. Sahmetlioglu, *ChemElectroChem* **2024**, *11*, e202300819.

[24] Y. Wang, X. Ge, Q. Lu, W. Bai, C. Ye, Z. Shao, Y. Bu, *Nat. Commun.* **2023**, *14*, 6968.

[25] R. Mohanty, A. Nashim, K. Parida, K. Parida, *Langmuir* **2024**, *40*, 14197.

[26] S. Panda, K. Deshmukh, S. K. Pasha, J. Theerthagiri, S. Manickam, M. Y. Choi, *Coord. Chem. Rev.* **2022**, *462*, 214518.

[27] S. A. Kadam, K. P. Kadam, N. R. Pradhan, *J. Mater. Chem. A* **2024**, *12*, 17992.

[28] S. Sahani, H. Mahajan, S. S. Han, *J. Energy Storage* **2024**, *90*, 111808.

[29] G. Rani, R. Ahlawat, H. Kumar, *J. Power Sources* **2024**, *617*, 235170.

[30] M. Lai, K. Chen, D. Wang, P. Cai, L. Sun, K. Zhang, B. Li, C. Yuan, Y. Zou, Z. Wang, *Mater. Today Nano* **2024**, *25*, 100450.

[31] S. M. Varghese, S. V. Mohan, S. Suresh, E. B. Gowd, R. B. Rakhi, *J. Alloys Compd.* **2024**, *973*, 172923.

[32] W. Wang, G. Chen, W. Kong, J. Chen, L. Pu, J. Gong, H. Zhang, Y. Dai, *J. Energy Storage* **2024**, *86*, 111097.

[33] A. Qayyum, M. O. Rehman, F. Ahmad, M. A. Khan, S. M. Ramay, S. Atiq, *Solid State Ionics* **2023**, *395*, 116227.

[34] B. D. Cullity, R. Smoluchowski, *Phys. Today* **1957**, *10*, 50.

[35] C. E. Shuck, A. Sarycheva, M. Anayee, A. Levitt, Y. Zhu, S. Uzun, V. Balitskiy, V. Zahorodna, O. Gogotsi, Y. Gogotsi, *In MXenes*, Jenny Stanford Publishing **2023**, pp. 539–560.

[36] S. Yan, R. Huang, H. Liu, S. Luo, *ACS Appl. Energy Mater.* **2024**, *7*, 6827.

[37] K. Moorthi, B. Sivakumar, B. Chokkiah, H. Valdes, S. Mohan, *ACS Appl. Nano Mater.* **2024**, *7*, 18511.

[38] N. Elgrishi, K. J. Rountree, B. D. McCarthy, E. S. Rountree, T. T. Eisenhart, J. L. Dempsey, *J. Chem. Educ.* **2018**, *95*, 197.

[39] S. Zhu, H. Tao, Y. Liu, X. Ma, K. Wang, Y. Wang, *J. Phys. Chem. B* **2022**, *126*, 10913.

[40] R. Wang, S. Wang, X. Peng, Y. Zhang, D. Jin, P. K. Chu, L. Zhang, *ACS Appl. Mater. Interfaces* **2017**, *9*, 32745.

[41] Z. Wang, M. T. Sougrati, Q. Zheng, R. Ge, J. Wang, *ACS Appl. Mater. Interfaces* **2024**, *16*, 18908.

[42] P. Cai, K. Wang, T. Wang, H. Li, M. Zhou, W. Wang, K. Jiang, *Adv. Energy Mater.* **2024**, *14*, 2401183.

[43] N. Díez, M. Sevilla, *ChemElectroChem* **2024**, *11*, e202300475.

[44] F. Meng, Y. Liu, Z. Ding, L. Xu, H. Wang, X. Xu, X. Liu, T. Lu, L. Pan, *Small* **2024**, *20*, 2309353.

[45] X. Shi, H. Wang, Z. Xie, Z. Mao, T. Zhang, J. Jin, B. He, R. Wang, Y. Gong, H. J. Fan, *Adv. Mater.* **2024**, *36*, 2406794.

[46] Z. Hao, Z. Meng, X. Li, X. Sun, J. Xu, H. Nan, W. Shi, G. Qi, X. Hu, H. Tian, *J. Colloid Interface Sci.* **2022**, *617*, 430.

[47] S. S. Pradeepa, K. Sutharthani, Y.-P. Fu, M. Sivakumar, *J. Energy Storage* **2024**, *98*, 112821.

[48] L. Liu, G. Liu, S. Wu, J. He, Y. Zhou, M. Demir, R. Huang, Z. Ruan, G. Jiang, P. Ma, *Ceram. Int.* **2024**, *50*, 1970.

[49] A. Elmushyakhi, B. Alqahtani, *J. Energy Storage* **2024**, *92*, 112289.

[50] M. Ali, A. W. Alrowaily, N. Drissi, B. M. Alotaibi, H. A. Alyousef, A. M. A. Henaish, *J. Phys. Chem. Solids* **2024**, *190*, 111973.

[51] K. A. Geelani, B. M. Alotaibi, A. W. Alrowaily, H. A. Alyousef, M. F. Alotiby, M. Abdullah, A. Dahshan, *J. Energy Storage* **2024**, *85*, 111054.

[52] C. Valentini, V. Montes-García, L. Cusin, D. Pakulski, M. Wlazło, P. Samorì, A. Ciesielski, *Small Sci.* **2024**, *4*, 2400031.

[53] M. S. Ali Akbari, S. Nandy, K. H. Chae, M. M. Najafpour, *J. Phys. Chem. Lett.* **2024**, *15*, 3591.

[54] S. Shen, Y. Lin, C. Liu, *Can. J. Chem. Eng.* **2024**, *102*, 1020.

[55] Q. Zhou, A. Griffin, J. Qian, Z. Qiang, B. Sun, C. Ye, M. Zhu, *Adv. Funct. Mater.* **2024**, *46*, 2405962.

[56] P. He, Y. Long, C. Fang, C. H. Ahn, A. Lee, C.-M. Chen, J. H. Park, M. Wang, S. K. Ghosh, W. Qiu, *Nano Energy* **2024**, *128*, 109858.

[57] M. Shahzad, F. Ahmad, M. Ibraheem, A. Shakoor, S. M. Ramay, M. R. Raza, S. Atiq, *RSC Adv.* **2025**, *15*, 6308.

[58] P. R. Sørensen, T. Jacobsen, *Electrochim. Acta* **1982**, *27*, 1671.